Precambrian Research 366 (2021) 106424

Contents lists available at ScienceDirect

Precambrian Research

journal homepage: www.elsevier.com/locate/precamres

Evolution of the Columbia supercontinent: Insights from the North Qilian Block, NW China

Yi-Xin Liu [a,b], Jin-Rong Wang [c], Yi-Wei Liu [d], Xiu-Quan Miao [a,b,e,*], Jian-Lin Chen [a,b,*]

[a] State Key Laboratory of Isotope Geochemistry, Guangzhou Institute of Geochemistry, Chinese Academy of Sciences, Guangzhou 510640, China
[b] CAS Center for Excellence in Deep Earth Science, Guangzhou 510640, China
[c] Key Laboratory of Mineral Resources in Western China (Gansu Province), School of Earth Sciences, Lanzhou University, Lanzhou 730000, China
[d] Second Institute Geological and Mineral Exploration of Gansu Provincial Bureau of Geology and Mineral Resources, Lanzhou 730000, China
[e] University of Chinese Academy of Sciences, Beijing, 100049, China

ARTICLE INFO

Keywords:
North Qilian Block
Lithospheric evolution
Proterozoic
Columbia supercontinent

ABSTRACT

The North Qilian Orogenic Belt, NW China, is surrounded by the Tarim and North China cratons to the northwest and northeast, respectively. The North Qilian Block (NQB) is preserved as Precambrian continental fragments in this belt. This block records a series of intense Proterozoic tectono–magmatic events associated with the convergence and breakup of the Columbia supercontinent, providing insights into the location of the block within this supercontinent. This study focuses on the Paleoproterozoic (*ca.* 1.74 Ga) amphibolites of the Beidahe Group (BDHG), and Mesoproterozoic (1.6–1.2 Ga) basalts of the Aoyougou (AF) and Huashugou (HF) formations of the Zhulongguan Group, all of which outcrop in the NQB.

The BDHG amphibolites have island arc basalt-type geochemical affinities with variable $\varepsilon_{Nd}(t)$ (−7.8 to −0.7) and $\varepsilon_{Hf}(t)$ (−9.8 to −2.1) values, that are indicative of the derivation from metasomatized mantle wedge in a continental arc setting. The ocean island basalt-like AF basalts and some HF basalts have depleted and decoupled Nd–Hf isotopic compositions ($\varepsilon_{Nd}(t) = 1.8–6.4$ and $\varepsilon_{Hf}(t) = 2.1–10.7$), and high mantle potential temperatures of up to 1642 °C, indicating derivation from a mantle plume in an intracontinental rifting setting. The normal mid-ocean-ridge basalt-like HF basalts originated from depleted asthenospheric mantle in a nascent ocean basin, as indicated by their Nd–Hf isotopic compositions ($\varepsilon_{Nd}(t) = 8.6–11.6$ and $\varepsilon_{Hf}(t) = 14.7–15.2$).

Combining these new data with the results of previous research, it is suggested that the Paleo–Mesoproterozoic evolution of the NQB involved paleo-oceanic plate subduction, intracontinental rifting, and the development of an embryonic oceanic basin, all of which were responses to Columbia supercontinent aggregation and breakup. The formation ages of the BDHG (*ca.* 1.74 Ga) and the AF (1.56–1.53 Ga) and detrital zircon ages (1.77 and 1.59 Ga) for the North Qilian Orogenic Belt are similar to those of the North China Craton (1.76 and 1.59 Ga) located to the southwest of the central Columbia supercontinent (i.e., Laurentia). This suggests that the NQB was located to the southwest of the Laurentia with volcanic islands within the Columbia supercontinent.

1. Introduction

Supercontinent amalgamation and dispersal cycles have dominated the evolution of continental blocks since at least the early Proterozoic. The Columbia (also termed Nuna) supercontinent is the earliest recognized Precambrian supercontinent (Zhao et al., 2004) and formed at 2.1–1.8 Ga before undergoing breakup at 1.6–1.2 Ga, as evidenced by the development of widespread mafic dike swarms (e.g., Pidgeon and Nemchin, 2001; Rogers and Santosh, 2009; Ernst and Bell, 2010; Zhao et al., 2016). This means that Precambrian mafic rocks formed at this time can provide insights into the evolution of the Columbia supercontinent. The North Qilian Block (NQB) is a Precambrian block that was broken up and is preserved as Precambrian continental fragments in the North Qilian Orogenic Belt, an early Paleozoic orogenic belt located in NW China that formed as a result of orogenesis after the Neoproterozoic. The Precambrian continental fragments are divided into the Beidahe (BDH) and Zhulongguan groups, and record the Proterozoic tectonic evolution of the NQB (e.g., Hou et al., 2008). However, the formation

* Corresponding authors at: State Key Laboratory of Isotope Geochemistry, Guangzhou Institute of Geochemistry, Chinese Academy of Sciences, Guangzhou 510640, China.
E-mail addresses: miaoxiuquan@gig.ac.cn (X.-Q. Miao), lzdxchen@gig.ac.cn (J.-L. Chen).

https://doi.org/10.1016/j.precamres.2021.106424
Received 8 May 2021; Received in revised form 5 September 2021; Accepted 2 October 2021
Available online 20 October 2021

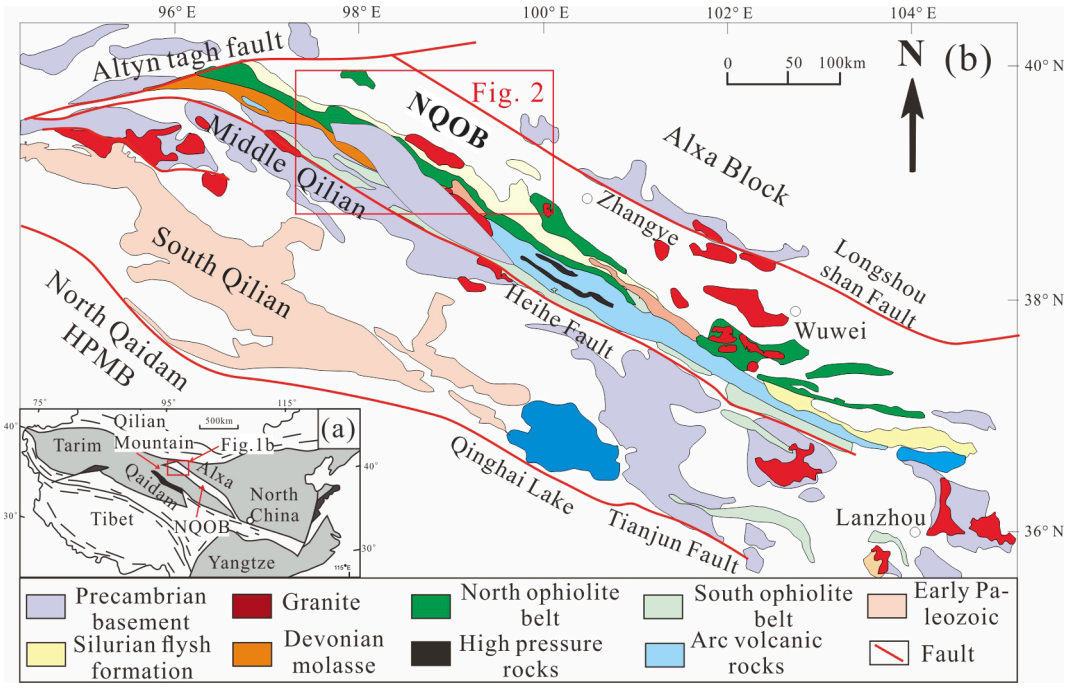

Fig. 1. (a) Tectonic location of the Qilian–Qaidam blocks in NW China (after Song et al., 2013); (b) the northwestern Qilian Block tectonic unit and Precambrian stratigraphic distribution map (modified after Wang et al., 2018; Xu et al. 2015).

age and tectonic setting of these fragments remain controversial. They are thought to have formed during either the Paleoproterozoic, Mesoproterozoic, or Paleozoic in various tectonic settings, including intracontinental rift and/or magmatic arc settings or combinations thereof (Supplemental Table 1). The relationship between the tectonic evolution of the NQB and the Columbia supercontinent also remains unclear, meaning that identifying the link would further our understanding of the evolution of the Columbia supercontinent.

The Laurentia was located in the central part of the Columbia supercontinent with the Siberia and Baltica to the north and northeast, respectively (e.g., Rogers and Santosh, 2009; Zhang et al., 2012). The nature of the western and southwestern borders of Laurentia remains controversial, with reconstructions placing the East Antarctica, Australia, Siberia, North China, or South China blocks in this location (Zhang et al., 2012; Hou et al., 2008). However, the location of the NQB within the Columbia supercontinent remains uncertain.

This paper presents new geochronological, geochemical, and isotopic data for (meta-)mafic rocks of the Precambrian BDH and Zhulongguan groups, both of which crop out across the western part of the North Qilian Orogenic Belt. Combining these new data with the results of previous research provides insights into (a) the petrogenesis of these units, (b) the Proterozoic tectono–magmatic evolution of the NQB and its relationship to the formation and breakup of the Columbia supercontinent, and (c) the location of the NQB within the Columbia supercontinent.

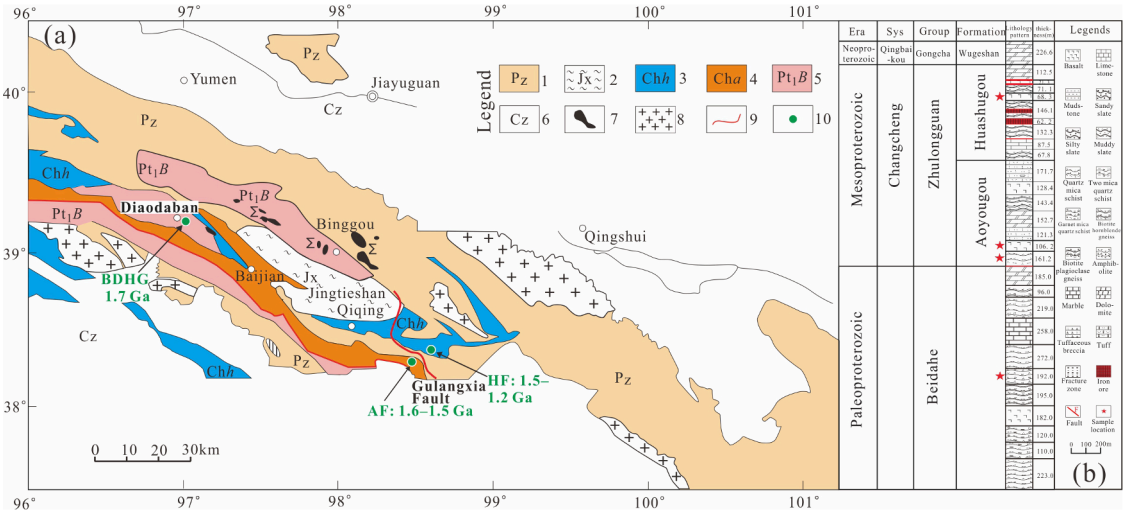

Fig. 2. (a) Geological map of the western North Qilian Orogenic Belt, NW China (modified from Qi et al., 2015) and (b) lithology histogram of Precambrian continental crust remnants. 1, Paleozoic; 2, Qingbaikou System; 3, HF, Zhulongguan Group, Changcheng Period; 4, AF, Zhulongguan Group, Changcheng Period; 5, BDHG, Paleoproterozoic; 6, Cennzoic; 7, Mafic–ultramafic rocks; 8, Intermediate–acid intrusion; 9, Fault; 10, Sampling site.

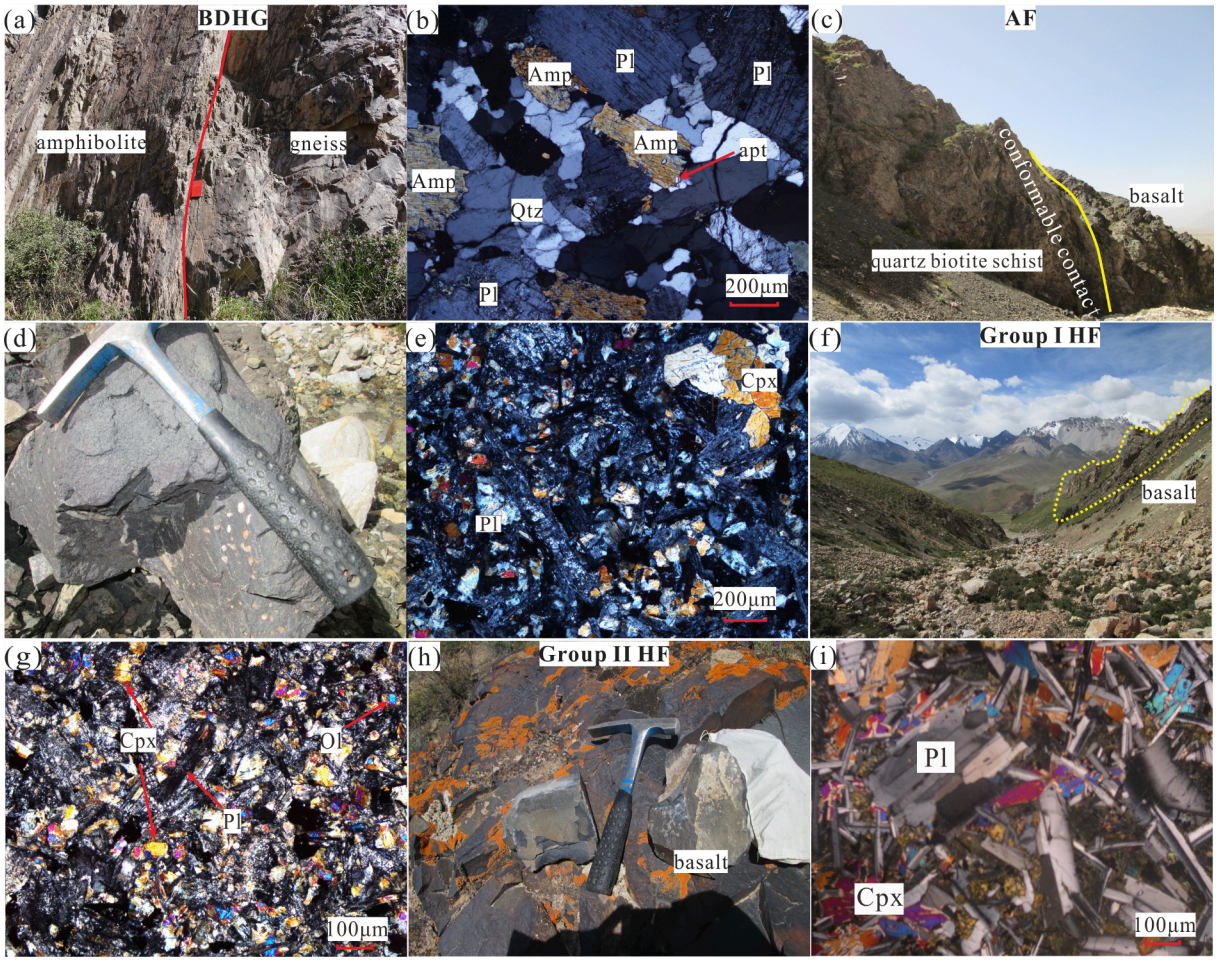

Fig. 3. (a, b) Field and photomicrographs of the BDHG amphibolites; (c) quartz biotite schists are in conformable contact with AF basalts; (d) hand specimen of the AF basalts; (e) photomicrographs of AF basalts; and (fi) field and photomicrographs of the HF basalts. Amp: amphibole; Pl, plagioclase; Apt, apatite; Cpx, clinopyroxene; Cb, carbonate; Ol, olivine.

2. Geological background and petrographic descriptions

2.1. Geological background

The WNW–ESE-striking Qilian Orogenic Belt is located in the northeastern margin of the Tibetan Plateau and forms part of the Central China Orogenic Belt. It is split from north to south into the North Qilian Orogenic Belt, the Middle Qilian Block, and the South Qilian Block (Fig. 1; e.g., Song et al., 2013). The North Qilian Orogenic Belt is an elongate, NW–SE-trending belt located along the junction of the three major geological blocks in China and is bound to the northwest by the Alxa Block of the North China Craton (Fig. 1). The western and northern boundaries of the North Qilian Orogenic Belt are the sinistral strike-slip Altyn Tagh Fault and the Longshoushan Fault, respectively (Fig. 1b). The belt is dominated by Paleozoic rocks and is thought to represent an early Paleozoic oceanic suture zone that separates the Alxa Block to the north from the Middle Qilian Block to the south (Fig. 1b). This area contains Paleozoic ophiolite sequences, high pressure/low temperature (HP/LT) metamorphic belts, volcanic rocks, granitoid plutons, flysch and molasse units, and a Carboniferous to Triassic sedimentary cover sequence (Song et al., 2013), all of which developed on a Precambrian block; i.e., the NQB. The NQB is split into continental fragments that formed as a result of post-Neoproterozoic orogenesis and is preserved as the Precambrian basement of the North Qilian Orogenic Belt. The Precambrian continental fragments are subdivided into the BDH and Zhulongguan groups, all of which contain amphibolite, schist, marble, gneiss, and conglomerate units that are intercalated with minor amounts of volcanic rocks (Fig. 1b; Yang et al., 2016). The lowermost BDH Group (BDHG) formed during the Paleoproterozoic (2001–1771 Ma) or Mesoproterozoic (1336–1166 Ma) (Supplemental Table 1) and is the oldest Precambrian basement material in the North Qilian Orogenic Belt. The widely distributed Zhulongguan Group is further divided into the Aoyougou (AF) and Huashugou (HF) formations (Fig. 2). The formation age of the Zhulongguan Group is controversial, with suggestions including early Mesoproterozoic (1529 Ma), late Neoproterozoic (600–580 Ma), and Paleozoic (504–480 Ma) ages (Supplemental Table 1). Yu (1997) proposed that the age boundary between the AF and the HF occurs at 1529 Ma.

The study area lies in the Diaodaban–Gulangxia region of the western North Qilian Orogenic Belt and includes outcrops of the BDH and Zhulongguan groups (Fig. 2a). The NW–SE-trending BDHG is exposed mainly in the Diaodaban and Binggou areas with a thickness of 1–4 km and a length of ~120 km (Fig. 2a). The BDHG exhibits intense structural deformation, including fold structures with gneissosity and schistosity. The BDHG comprises mainly amphibolite (metavolcanic rocks) and schist (metasedimentary rocks) with minor gneiss (Fig. 2b), recording low–middle-grade metamorphism of high-greenschist facies. The underlying BDHG is in fault contact with the overlying AF with a sudden change in lithology from dolomites to schists (Fig. 2b), indicating the absence of strata or change in sedimentary environment. The NW–SE-trending AF crops out mainly in the Baijian and southern Gulangxia Fault with a thickness of 3–7 km and length of ~120 km (Fig. 2a). Rock assemblages of the AF include dolomite, quartz biotite schist, basalt, and sedimentary rocks. Our field geological survey indicates that quartz

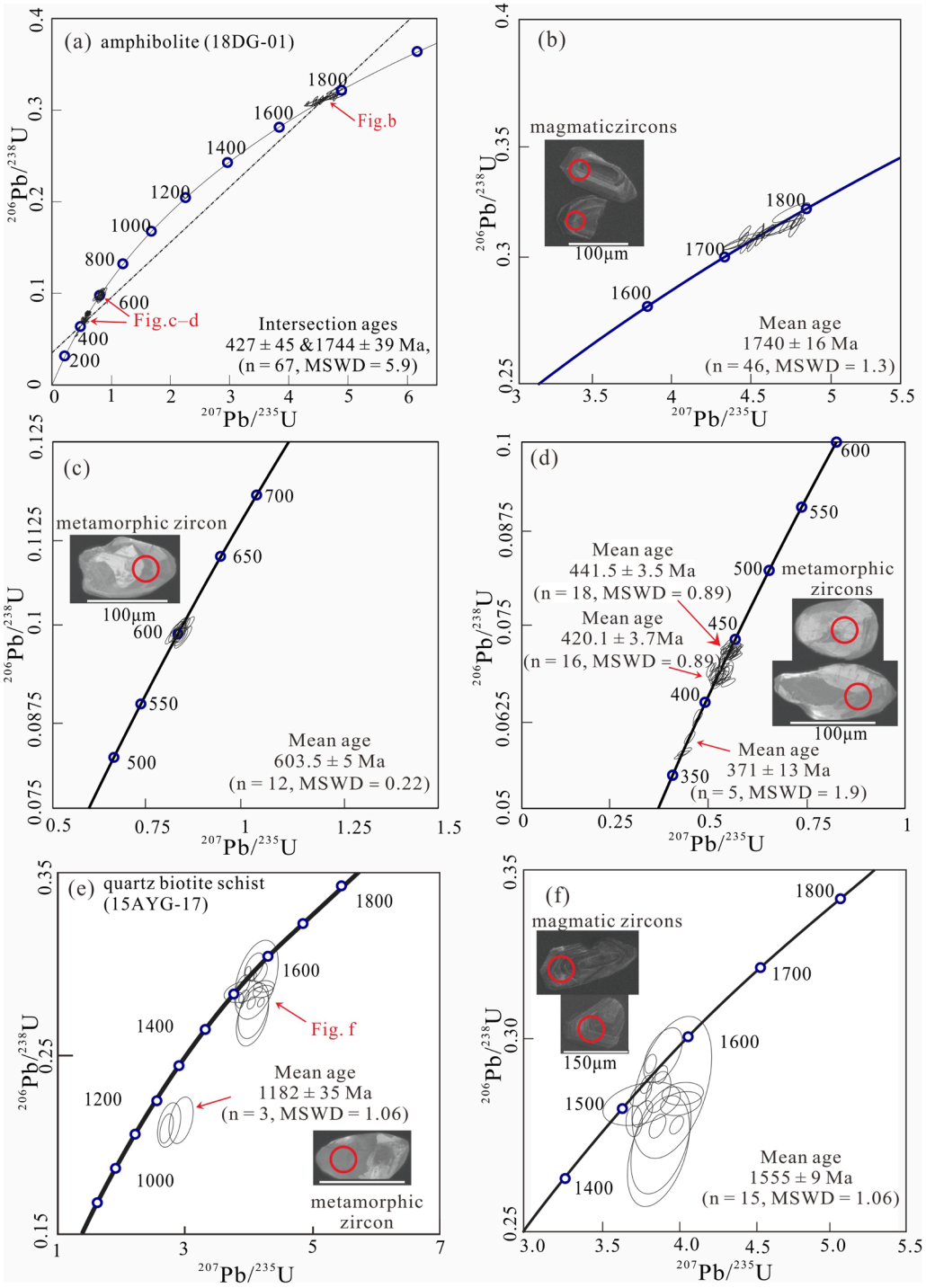

Fig. 4. Cathodoluminescence images of representative zircons and U–Pb concordia diagrams for zircons from BDHG amphibolite and AY quartz biotite schist.

biotite schists are in conformable contact with AF basalts (Fig. 2b, Fig. 3d). The near NW-striking HF conformably overlies the AF in the northern Gulangxia Fault (Fig. 2), which comprises mainly argillaceous slate–carbonate–banded iron with minor basalt (Fig. 2b).

2.2. Sample descriptions

Eighteen amphibole samples were collected from the BDHG in the Diaodaban area, and seven and ten basaltic samples from the AF and HF areas to the south and north of the Gulangxia Fault, respectively (Fig. 2b). The BDHG amphibolite is massive and contains amphibole (~50 vol%), plagioclase (~40 vol%), biotite, quartz, and accessory minerals (e.g., apatite; Fig. 3a, b). Most phenocrysts retain their original euhedral–subhedral forms with variable size (100–500 μm) and, together with their unifoliate minerals (Fig. 3a, b) indicate low-grade metamorphism. The AF basalts are in conformable contact with the underlying quartz-biotite schist and are massive, amygdaloidal, and granular (Fig. 3c, d). They contain subhedral–anhedral plagioclase (~20 vol%), clinopyroxene (~40 vol%), and olivine (~10 vol%) of various sizes (50–250 μm). The clinopyroxenes form clusters containing several clinopyroxene crystals (Fig. 3e). The HF basalts can be divided into two groups based on the results of optical microscopy. The Group I

are massive, granular, and contain variably sized euhedral–subhedral plagioclase (~35 vol%), clinopyroxene (~45 vol%), and olivine (~10 vol%; Fig. 3f, g). The Group II are massive and porphyritic and contain euhedral plagioclase (~40 vol%) and clinopyroxene (~20 vol%; Fig. 3h–i). The influence of later alteration on the AF and HF basalts was negligible, as indicated by the unaltered minerals (Fig. 3e, g, i).

3. Results

Details of the analytical methods used during this study are given in the Supporting Information, Appendix 1. Mineral and whole-rock geochemical data, Zircon U–Pb geochronological data for the BDHG amphibolites and AF quartz-biotite schists, and Sr–Nd–Hf isotope data for the BDHG amphibolites and AF and HF basalts are given in Supplemental Tables 2 and 3.

3.1. Zircon U–Pb ages

Zircon U–Pb dating was carried out on 67 grains from the BDHG amphibolite (sample 18DG–01) and 18 grains from the AF quartz-biotite schist (sample 15AYG–17). Of the 68 zircons from the BDHG amphibolite, 51 have elliptical or irregular shapes and have planar zoning visible during cathodoluminescence (CL) imaging (Fig. 4c, d). They contain low concentrations of Th and U and have low Th/U ratios (0.01–0.12; Supplemental Table 2), indicating a metamorphic origin. The remaining 16 zircons are euhedral–subhedral and prismatic and have oscillatory zoning visible during CL imaging (Fig. 4b). They have high concentrations of Th and U and high Th/U ratios (0.41–0.96; Supplemental Table 2), all of which indicate a magmatic origin. Magmatic zircons from the BDHG amphibolite yield $^{207}Pb/^{206}Pb$ ages from 1802 to 1687 Ma and a weighted mean age of 1740 ± 16 Ma, which is consistent with the upper intersect age defined by these zircons (1744 ± 39 Ma; Fig. 4a, b). The metamorphic zircons define four age groups with $^{206}Pb/^{238}U$ weighted mean ages of 604 ± 5 (Fig. 4c), 442 ± 4, 420 ± 4, and 371 ± 13 Ma (Fig. 4d).

Zircons from the AF quartz-biotite schist have both metamorphic and magmatic origins. Of the 18 grains analyzed, 15 are of metamorphic origin and have low concentrations of Th and U, low Th/U ratios (0.07–0.10), and yield a $^{207}Pb/^{206}Pb$ weighted mean age of 1182 ± 35 Ma (Supplemental Table 2; Fig. 4e). The magmatic zircons have clear oscillatory zoning visible during CL imaging (Fig. 4f), high concentrations of Th and U, and high Th/U ratios (0.31–1.36; Supplemental Table 2), and yield $^{207}Pb/^{206}Pb$ ages from 1575 to 1513 Ma and a weighted mean age of 1555 ± 9 Ma (Fig. 4f).

3.2. Mineral compositions

The apatites of the BDHG amphibolite are enriched in F (1.78–2.96 wt%) but depleted in Cl (0.01–0.12 wt%) and are classified as fluorapatite (Supplemental Table 4).

Clinopyroxenes in the AF basalt comprise Wo (18.8–28.2), En (45.5–62.7), and Fs (9.50–33.5), with $Mg^{\#}$ values of 60.5–86.3, and are augites (Supplemental Table 5).

3.3. Major and trace elements

All of the samples analyzed during this study have high loss on ignition (LOI) values (up to 7.27 wt%) that meant all major element data were recalculated on an anhydrous basis prior to interpretation. The BDHG amphibolites (samples 18DG–01–18) have variable SiO_2 (45.1–50.5 wt%), MgO (3.52–9.39 wt%), and TiO_2 (1.02–3.55 wt%) contents, high Na_2O (1.36–3.92 wt%) contents, relatively low K_2O (0.14–1.61 wt%) contents, and $Mg^{\#}$ values of 26.8–52.8 (where $Mg^{\#} = Mg^{2+}/(Mg^{2+}+Fe^{2+}) \times 100$). The AF basalts have less variable SiO_2 (48.2–51.4 wt%), TiO_2 (2.10–3.12 wt%), and MgO (5.75–7.21 wt%) contents and $Mg^{\#}$ values (49.9–53.4), relatively high K_2O (4.59–6.60 wt%) contents, relatively low Na_2O (1.17–2.76 wt%) contents, and low K_2O/Na_2O values (1.66–5.62). The HF basalts have relatively low SiO_2 (41.7–45.3 wt%) contents and high MgO (6.90–8.76 wt%) contents, with $Mg^{\#}$ values of 54.5–65.9. Group I HF basalts have higher K_2O (3.15–3.41 wt%) and total alkali (5.96–6.32 wt%) contents relative to the Group II HF basalts, which have relatively low K_2O (0.06–0.08 wt%) and total alkali (0.29–0.31 wt%) contents. The protoliths of the BDHG amphibolites and the Group II HF basalts are classified as subalkaline basalts in a Zr/TiO_2 versus Nb/Y diagram (Fig. 5), whereas the AF and Group I HF basalts have alkaline basalt protoliths.

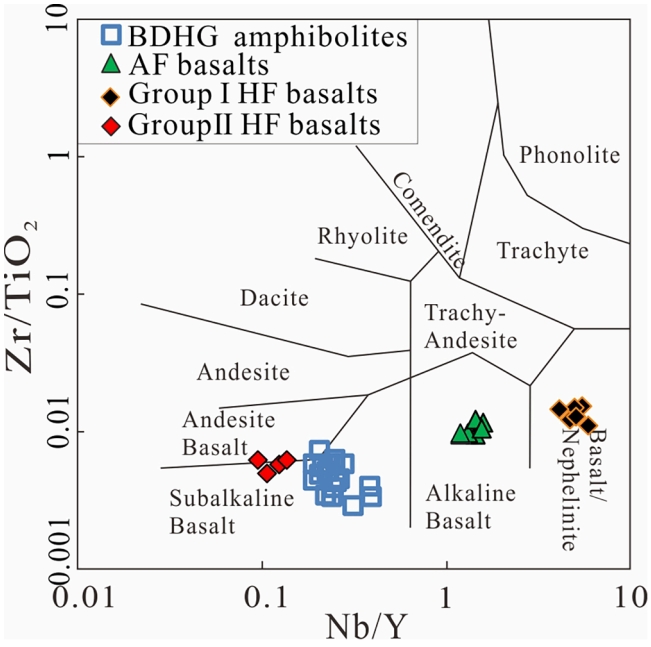

Fig. 5. Nb/Y vs. Zr/TiO_2 lithology classification diagram (after Winchester and Floyd, 1976).

The studied samples are enriched in light rare earth elements (LREEs; $(La/Yb)_N$ = 2.13–3.16, 6.92–9.44, and 27.6–31.2, respectively; Fig. 6) with the exception of the Group II HF basalts ($(La/Yb)_N$ = 1.33–1.42). The BDHG amphibolites have negative Eu and Ce anomalies (δEu = 0.76–0.87, barring one sample with a δEu value of 1.01; δCe = 0.78–0.82). They have primitive mantle-normalized multi-element variation diagram patterns that are characterized by positive Rb, Th, U, and Pb and negative Nb, Ta, and Ti anomalies, indicating they are compositionally similar to island arc basalts (IAB; Fig. 6a, b). In comparison, the AF and Group I HF basalts are depleted in large ion lithophile elements (LILEs; e.g., Pb, Sr) and enriched in high field strength elements (HFSEs; e.g., Nb, Ta), indicating that they have ocean island basalt (OIB)-type compositions (Fig. 6c, f). The Group II HF basalts are depleted in LILEs but slightly enriched in HFSEs, suggesting they have a normal mid-ocean ridge basalt (N-MORB)-type affinity (Fig. 6c, f).

3.4. Whole-rock Sr–Nd and Lu–Hf isotopic compositions

The BDHG amphibolites are characterized by variable and enriched Sr, Nd, and Hf isotopic compositions with $(^{87}Sr/^{86}Sr)_i$ = 0.70683–0.70899, $\varepsilon_{Nd}(t)$ = −7.8 to 0.7, and ($\varepsilon_{Hf}(t)$ = −9.8 to 2.1 (Fig. 7). The $(^{87}Sr/^{86}Sr)_i$, $\varepsilon_{Nd}(t)$ and $\varepsilon_{Hf}(t)$ of the AF basalts range from 0.70546 to 0.70843, 1.8 to 5.5 and 4.1 to 9.0, respectively. For the Group I and II HF basalts, $(^{87}Sr/^{86}Sr)_i$ = 0.70434–0.70637 and 0.70131–0.70236, $\varepsilon_{Nd}(t)$ = 4.7–6.4 and 8.6–11.6, and $\varepsilon_{Hf}(t)$ = 2.1–10.7 and 14.7–15.2, respectively (Fig. 7).

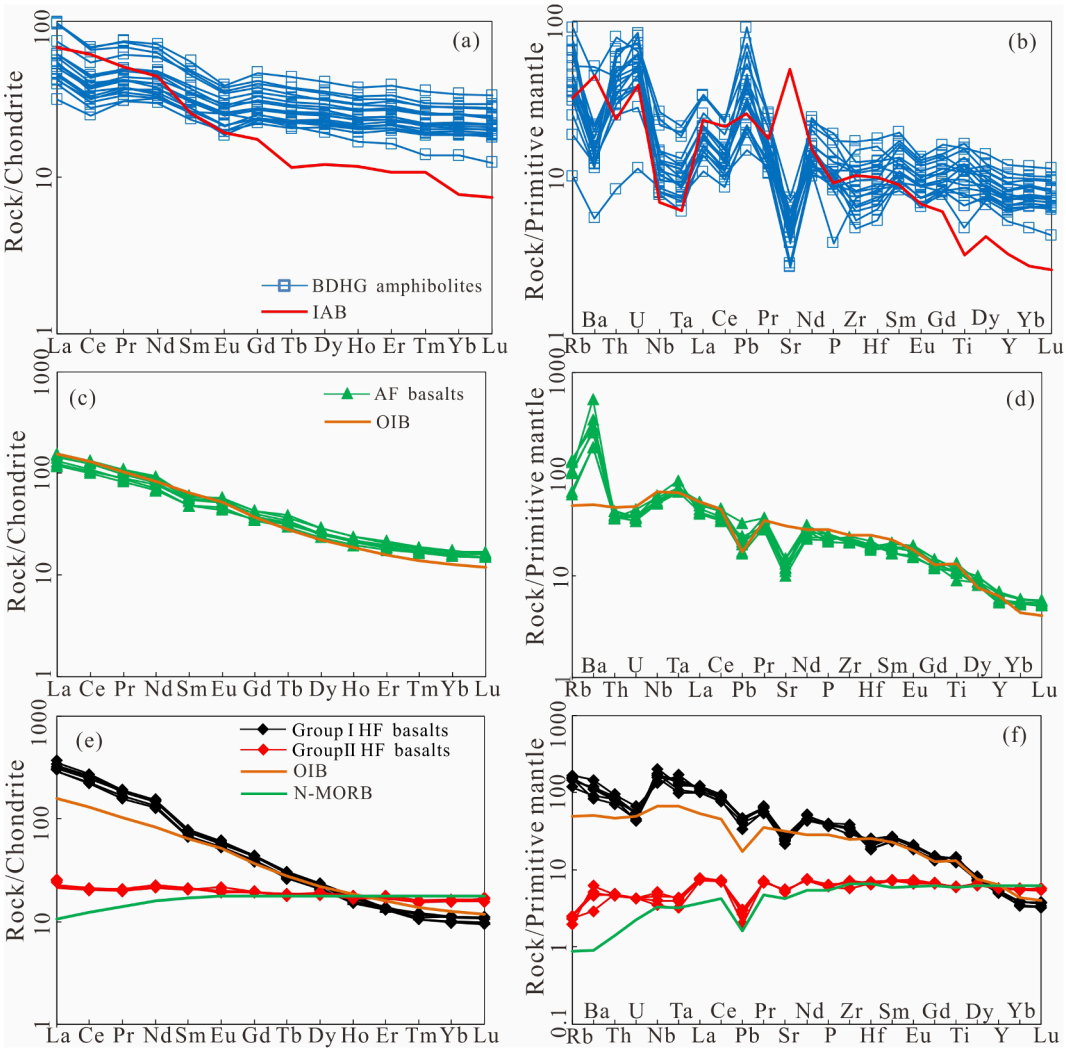

Fig. 6. Chondrite-normalized rare-earth-element patterns and primitive-mantle-normalized trace-element spider diagrams for the BDHG amphibolites, and AF and HF basalts. Chondrite, primitive-mantle, OIB, and N-MORB values are after Sun and McDonough (1989); the IAB value is the average for Aleutian island arc basalt, after Kelemen et al. (2003).

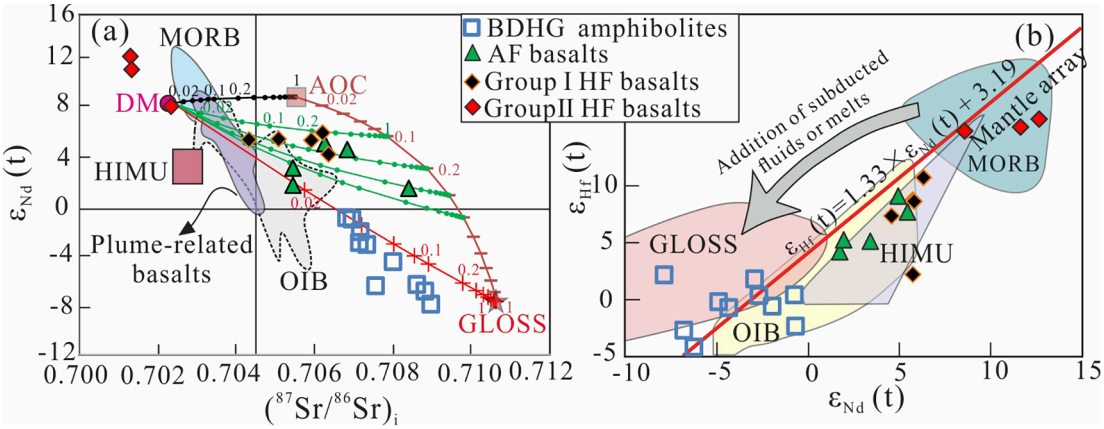

Fig.7. (a) $(^{87}Sr/^{86}Sr)_i$ vs. ε_{Nd} (t) and (b) ε_{Nd} (t) vs. ε_{Hf} (t) diagrams. For the mantle array, ε_{Hf} (t) = 1.33 × ε_{Nd} (t) + 3.19 (Kempton et al., 2002). The data for HIMU, EM I, EM II, MORB, OIB, GLOSS, and plume related basalts are from the references listed in the supporting information of Appendix 1. The $(^{87}Sr/^{86}Sr)_i$ ratios and ε_{Nd}(t) and ε_{Hf}(t) values for the DM, AOC, GLOSS are given in Supplemental Table 7.

4. Discussion

4.1. Effects of alteration and Low-Grade metamorphism

The BDHG has undergone metamorphism and alteration as evidenced by the high LOI values (up to 7.27 wt%) of the Zhulongguan Group basalts (Supplemental Table 3). This means that the potential effects of metamorphism and alteration need to be assessed before interpreting the compositions of these units. The HFSEs (e.g., Zr, Nb) are generally immobile during alteration and metamorphism, especially when compared with the easily mobilized LILEs and REEs (e.g., Polat and Hofmann, 2003). As such, we focus on the HFSEs to evaluate the mobility of the other trace elements during the metamorphism and alteration recorded in the study area. Element mobility was assessed by plotting potentially mobile elements in bivariate diagrams with Nb (or Zr), where immobile incompatible elements would typically define positive linear trends if their concentrations are only controlled by magmatic processes (e.g., Polat and Hofmann, 2003). Plotting data for the BDHG amphibolites and the AF and HF basalts indicates that U, La, and Zr all positively correlate with Nb whereas Rb does not correlate with Nb (Supplemental Fig. 1), indicating that the LILE concentrations have been modified by alteration or metamorphism. In comparison, the REE and HFSE concentrations in the BDHG amphibolites and the AF and HF basalts reflect magmatic processes. In addition, it is unlikely that SiO_2 was mobile under the P–T conditions of metamorphism in the study area, as evidenced by the lack of correlation between the SiO_2 contents and LOI values of the BDHG amphibolites (Supplemental Fig. 1). This is consistent with the generally low-grade metamorphic conditions recorded by these samples, as evidenced by the fact that some of the amphibole and plagioclase phenocrysts retain their igneous euhedral–subhedral textures (Fig. 3a, b). This means that only the LILE concentrations have been influenced by metamorphism and alteration, with all other elements being potentially useful for determining the petrogenesis, source, and tectonic setting of the magmatism.

4.2. Assimilation and fractional crystallization

Some of the samples have low $Mg^{\#}$ values and contain high K_2O and LILE contents (Supplemental Table 3), all of which suggests that the magmas that formed these samples assimilated crustal material prior to emplacement or eruption. Continental crustal material has low Nb/U (~6.2), Sm/Nd (~0.87), and $\varepsilon_{Nd}(t)$ values, high La/Sm (~6.6) values, and high SiO_2 contents (Rudnick and Fountain, 1995). However, all of the studied samples have Nb/U ratios higher than those expected for the continental crust (75.3–9.4). In addition, their La/Sm (or $\varepsilon_{Nd}(t)$ and Sm/Nd) values do not correlate with variations in their SiO_2 contents, suggesting negligible crustal contamination (Supplemental Fig. 2).

In general, mantle-derived primary melts have Ni concentrations > 400 ppm, Cr concentrations > 1000 ppm, and $Mg^{\#}$ values of 73–81 (Litvak and Poma, 2010). The low $Mg^{\#}$ values (27–66) and Ni concentrations (19.5–144 ppm) and variable Cr concentrations (123–2296 ppm; Supplemental Table 3) of the studied samples suggest they were derived from parental magmas that fractionated significant amounts of Mg-rich minerals such as olivine and clinopyroxene. Here we use partition coefficients for various elements in different minerals to define covariant diagrams for Ni (Sc/Yb, Nb/Ta, and CaO/Al_2O_3) relative to MgO (Supplemental Fig. 3). Combined with their δEu values, these suggest that the protoliths of the BDHG amphibolites fractionated olivine, clinopyroxene, and plagioclase (δEu = 0.76–0.87) prior to their emplacement or eruption. Their positive Ti anomalies and the presence of a positive correlation between La/Sm values and TiO_2 contents indicate that the BDHG amphibolites record the accumulation of titanium rich minerals (e.g., amphibole, not shown; Brenan et al., 1995). In comparison, the AF basalts record the fractional crystallization of olivine and clinopyroxene, whereas the Hf basalts record only fractional crystallization of clinopyroxene (Supplemental Fig. 4).

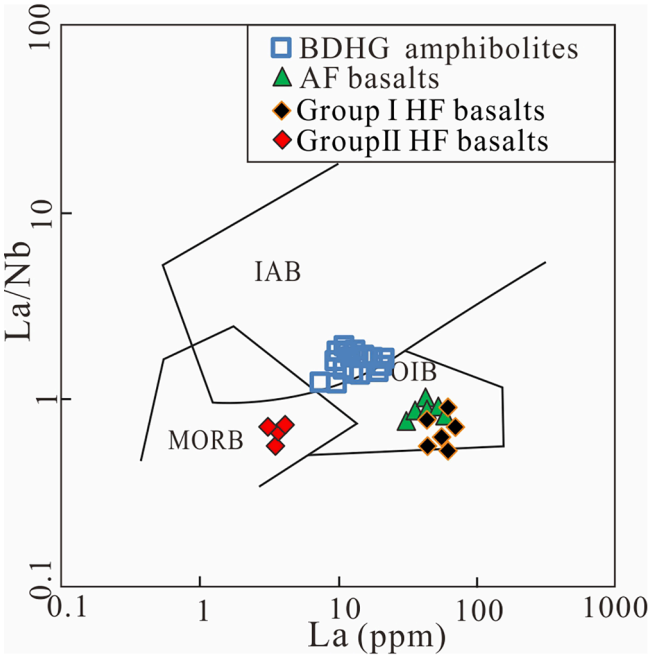

Fig. 8. La vs. La/Nb discrimination diagram.

4.3. Sources of the BDHG and Zhulongguan Group rocks

4.3.1. Protolith source for the BDHG amphibolites

The BDHG amphibolites have compositions with IAB-type affinities, as evidenced by their Rb and Pb enrichments, Nb and Ti depletions, and high La/Nb ratios (Fig. 8). Previous research suggests that IAB formed from magmas generated by the partial melting of mantle wedge material previously metasomatized by interaction with aqueous fluids and/or sedimentary melts derived from subducted slab material (i.e., mafic oceanic crust and overlying sediments; Merle et al., 2014). However, mafic oceanic crustal material is generally derived from the depleted mantle, indicating that fluids and/or melts derived from subducted oceanic crustal material cannot significantly modify the Sr–Nd–Hf isotopic compositions of depleted mantle wedges. This means that the relatively enriched Sr–Nd–Hf isotopic compositions and significant positive Pb anomalies of the BDHG amphibolites are indicative of metasomatism of a mantle wedge by fluids and/or melts derived from subducted sedimentary material. The BDHG amphibolites also have higher $(^{87}Sr/^{86}Sr)_i$ and lower U/Nb (0.04–0.20) values than aqueous fluids released from altered oceanic crustal material (AOC; $^{87}Sr/^{86}Sr$ = 0.70412, Nielsen and Marschall, 2017; U/Nb = 4.8, Kessel et al., 2005). This, together with the presence of a negative correlation between U/Nb ratios and Nd isotopes (Fig. 9a), further supports the involvement of fluids/melts derived from subducted sediments. It is important to note that Th is mobile during the melting of subducted sedimentary material with high Th/Nb values (0.77; Plank and Langmuir, 1998). The BDHG amphibolites have Th/Nb values that negatively correlate with their Nb/La values (Fig. 9b). This, combined with their negative Ce anomalies (Fig. 6a), suggests that they formed from magmas derived from a source region containing subducted sediment-derived melts (e.g., Kessel et al., 2005; Yogodzinski et al., 2015). This is consistent with the enriched and decoupled Nd–Hf isotopic compositions of these samples. Zircon, monazite and rutile are residual phases during partial melting of subducted sediments. A mantle source metasomatized by these sediment-derived melts would have decoupled Nd–Hf isotopic compositions (Tollstrup and Gill, 2005; Fig. 7b). Plotting the BDHG amphibolites on a two-component Sr–Nd isotopic mixing diagram for depleted mantle and subducted sedimentary material indicates that these samples were derived from magmas with mantle sources containing 4%–20%

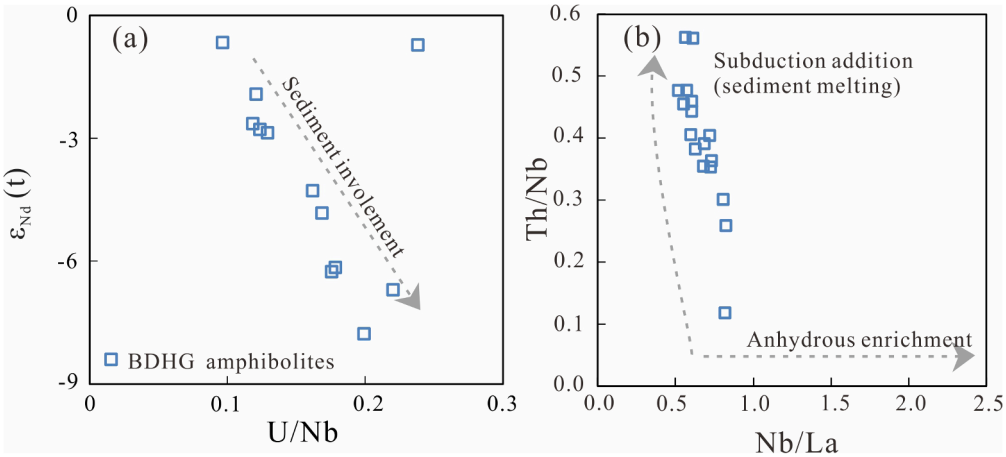

Fig. 9. (a) U/Nb vs. ε_{Nd} (t) and (b) Nb/La vs. Th/Nb diagram.

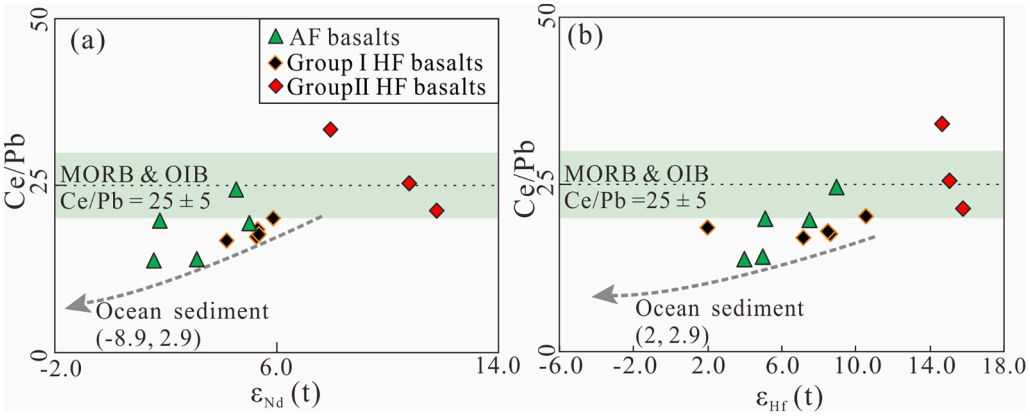

Fig.10. (a) ε_{Nd} (t) vs. Ce/Pb) and (b) ε_{Hf} (t) vs. Ce/Pb diagrams (the data for MORB and OIB are after Sun and McDonough (1989) and Haase and Devey (1996); and ocean sediments after Plank and Langmuir (1998).

subducted sedimentary material (Fig. 7a).

4.3.2. Source of the Zhulongguan Group basalts

The AF and Group I HF basalts are enriched in LREEs and HFSEs but have depleted Nb and Hf isotopic compositions and low La/Nb values (Figs. 6 and 8), all of which are indicative of OIB-type affinity. However, the Group II HF basalts have N-MORB-type affinity in that they are depleted in LILEs (Rb and Pb), have no negative HFSE anomalies (e.g., Nb, Ta and Ti), have low La/Nb values, and have depleted Nd and Hf isotopic compositions (Figs. 6–8).

It is generally considered that OIBs form from hot spots or mantle plumes incorporating subducted material (e.g., Jackson et al., 2007; Chauvel et al., 2008). The depleted Nd–Hf isotopic compositions of AF and Group I HF basalts are decoupled and lower than those of the mantle array (Fig. 7), indicating the involvement of subducted sediments (e.g., Jackson et al., 2007; Chauvel et al., 2008). The subducted sediments may be entrained in buoyant upwelling plumes and returned to Earth's surface at hotspots (e.g., Jackson et al., 2007). Furthermore, the mantle source of AF and Group I HF basalts has a high mantle potential temperature, as indicated by the high crystallization temperature of clinopyroxene in these samples (up to 1470 °C; Fig. 11; Supplemental Table 5). This is substantiated by the high estimated temperatures of the AF and Group I HF basalts at which melts separate from the melting column varies from 1484 °C to 1600 °C and 1518 °C to 1642 °C, as calculated using the methods of Lee et al. (2009) and Herzberg and Asimow (2015), respectively (Supplemental Table 6). A prerequisite for the formation of mantle plumes is a high mantle potential temperature

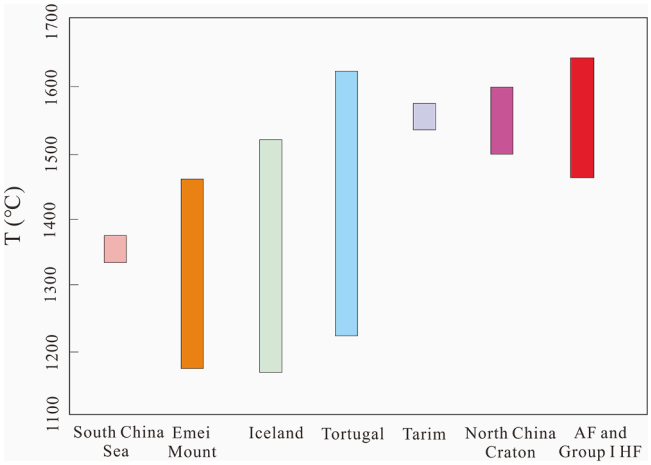

Fig. 11. The mantle potential temperature of AF and Group I basalts compared with the global mantle plume. Temperatures of South China Sea, Emei Mount, Iceland, and Tortugal mantle plumes are after Yang et al. (2019) and references therein, and for the Tarim and North China plume are after Zhang et al. (2017) and Peng et al. (2010).

(e.g., Xu et al., 2004). Thus, the AF and Group I HF basalts were generated by a mantle plume incorporating subducted oceanic crustal material. This is consistent with the positive relationship between their

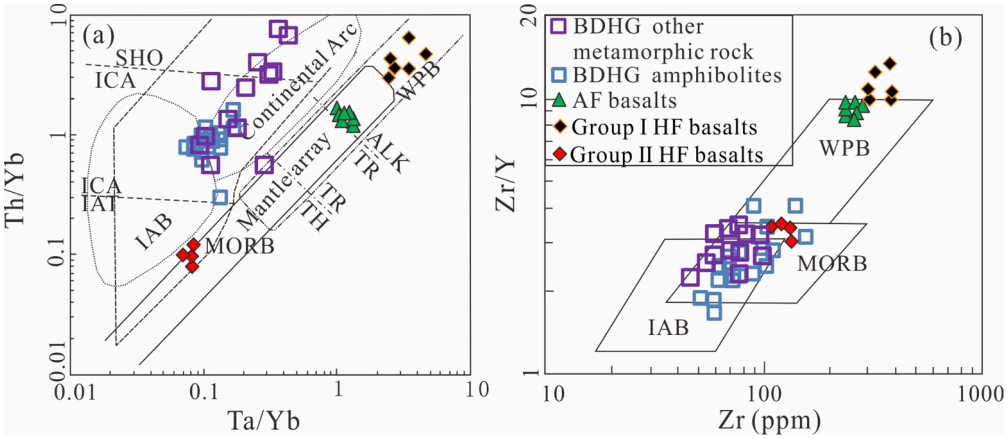

Fig. 12. Tectonic discrimination diagrams. (a) Ta/Yb vs. Th/Yb, after Rudnick and Fountain (1995); (b) Zr vs. Zr/Y, after Pearce and Norry, (1979). IAB, island arc basalt; MORB, mid-oceanic-ridge basalt; WPB, within-plate basalt; SHO, shoshonite; ICA, calc–alkaline basalt; IAT, island arc tholeiite; ALK, alkaline basalt; TH, tholeiite; TR, transitional basalt. The BDHG metamorphic rocks are after Gao (2003), Fu et al. (2005), and Nan (2018).

$\varepsilon_{Nd}(t)$ and $\varepsilon_{Hf}(t)$ or Ce/Pb values, all of which are indicative of the involvement of subducted sedimentary material in their petrogenesis (Fig. 10). Plotting the AF and Group I HF basalts in a three-component Sr–Nd isotopic mixing diagram indicates that these units were derived from a depleted asthenospheric mantle source containing 4%–15% subducted slab material with an AOC/sediment ratio between 90:10 and 70:30 (Fig. 7a).

The N-MORB-like Group II HF basalts also likely originated from depleted asthenospheric mantle material, as indicated by their depleted $\varepsilon_{Nd}(t)$ and $\varepsilon_{Hf}(t)$ isotopic compositions (Fig. 7) and low Gd/Yb (1.44–1.48), Zr/Y (3.82–4.13), and Ta/Yb (0.08) ratios.

4.4. Tectonic setting

4.4.1. Tectonic setting of the BDHG

The $^{207}Pb/^{206}Pb$ weighted mean age (1740 ± 16 Ma) of magmatic zircons from the BDHG amphibolite is indicative of the timing of formation of the protoliths for these units, which is consistent with previous research that suggested the BDHG formed during the Paleoproterozoic (1771–2001 Ma; Supplemental Table 1). Previous studies have suggested that the BDHG was formed in either an arc (Gao, 2003; Fu et al., 2005; Nan, 2018) or rift (e.g., Zhang and Mao, 1998) setting. The geochemical and isotopic compositions of the BDHG amphibolites supports formation in an arc-type setting for a number of reasons: (a) the BDHG amphibolites plot within continental arc and IAB fields of tectonic setting discrimination diagrams (Fig. 12), which is consistent with previous research on metamorphosed BDHG rocks that suggested they formed in a continental arc setting (Gao, 2003; Fu et al., 2005; Nan, 2018); (b) they have low Nb/U ratios (average 9.4) that are similar to those expected for continental arc volcanic rocks (Nb/U = ~12; Kelemen et al., 2003); and (c) the mantle source of the protoliths for BDHG amphibolites was metasomatized by interaction with subducted aqueous fluids and sediment-derived melts as discussed above.

The apatites in the BDHG amphibolites are euhedral prismatic crystals with low MnO contents, implying a magmatic origin (Fig. 13a). They therefore record the characteristics of the parental magma. The Mn and P concentrations of apatite in the BDHG amphibolites also negatively correlate, with apatite Mn + Si concentrations also negatively correlating with Ca + P concentrations (Fig. 13b, c). This indicates that the Mn in the apatite was incorporated as Mn^{5+} with a minor amount present as Mn^{3+}, suggesting that the apatite formed under high oxygen fugacity conditions around the magnetite–hematite buffer (Fig. 13d). Different tectonic settings are typically associated with variations in oxygen fugacity conditions, with subduction environments associated with high oxygen fugacities and intraplate environments associated with relatively low oxygen fugacity conditions (Frost and McCammon, 2008). This means that the high oxygen fugacity environment evidenced by the BDHG amphibolites is consistent with their formation in a continental arc environment.

The blocks surrounding the NQB also contain abundant Paleoproterozoic IAB-like (meta-)mafic rocks that formed in island arc environments, including the Dunhuang Block (Zhao et al., 2015), the Middle Qilian Block (Guo et al., 1999), and the North China Craton (Lu et al., 2010). All of this suggests that the BDHG amphibolites formed in a continental arc environment during the late Paleoproterozoic (1740 ± 16 Ma). Combining the metamorphic zircon U–Pb ages for the BDHG amphibolites (Fig. 4; 604 ± 5, 442 ± 4, 420 ± 6, and 371 ± 13 Ma) with the results of previous research on the North Qilian Orogenic Belt (Wang et al., 2005; Song et al., 2013) suggests that the belt most likely records tectonic events associated with the breakup of Rodinia (710–603 Ma), the closure of the Paleo–Qilian Ocean (*ca.* 440 Ma), a continent–continent collisional orogeny (*ca.* 420 Ma), and post–collisional extension (<400 Ma; Song et al., 2013).

4.4.2. Formation age and tectonic setting of the Zhulongguan Group

Previous studies have suggested that the Zhulongguan Group was formed either during the late Neoproterozoic (600–580 Ma; Xu et al., 2015) or the Paleozoic (504–480 Ma; Xiang et al., 2007; Xia et al., 2012). The study area contains the Paleozoic Aoyougou ophiolites that were either accreted onto or intruded the Precambrian units in the study area (Xiang et al., 2007; Song et al., 2013). Neoproterozoic or Paleozoic samples collected from the Aoyougou Valley or Jiugeqingyang (Xiang et al., 2007; Xia et al., 2012; Xu et al., 2015) could also be part of the Aoyougou ophiolite rather than the Precambrian units that were sampled during this study. The Zhulongguan Group is split into underlying AF and overlying HF units. Combining the new zircon U–Pb data presented in this study with field relationships and the results of previous research suggests that the AF formed during the Mesoproterozoic (1555–1529 Ma). This is evidenced by the fact that the younger AF is in faulted contact with the older underlying BDHG (1740 ± 16 Ma; Fig. 2b). In addition, the zircon U–Pb age for the AF quartz-biotite schist (1555 ± 9 Ma) constrains the oldest possible timing of formation of the AF basalts, as the schists conformably underlie the AF basalts (Fig. 2b). Yu (1997) also reported a 1529 Ma Sm–Nd isochron age for the AF basalts in the Subei area of the western North Qilian Orogenic Belt and reported this as an age boundary between the AF and the HF.

A zircon U–Pb age of 1235 Ma for diabase within the Jingtieshan Group, which conformably overlies the HF basalts (Yang et al., 2016), represents the youngest possible age of the HF. This age is consistent with the metamorphic age of 1182 Ma for the AF quartz-biotite schists,

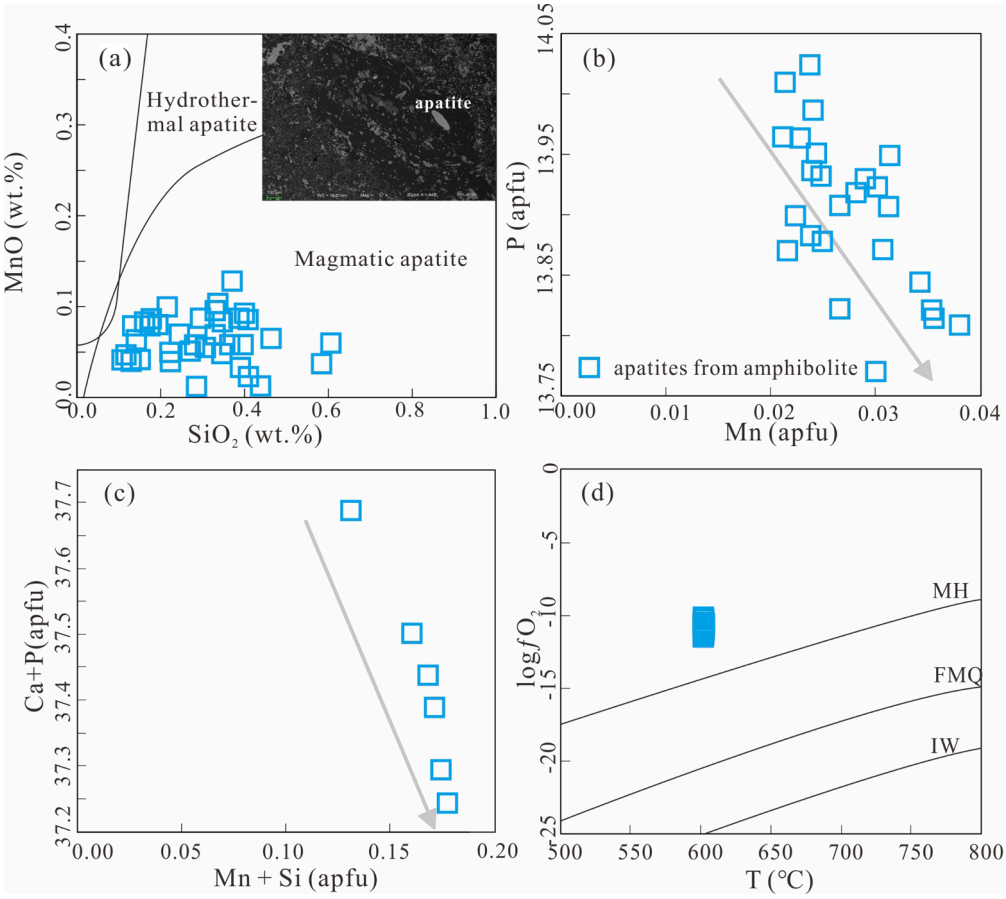

Fig. 13. (a) SiO_2 vs. MnO; (b) Mn vs. P; (c) (Mn + Si) vs. (Ca + P); and (d) $\log fO_2$ vs. T (°C) diagrams for the apatites in amphibolite. MH, magnetite–hematite buffer; FMQ, fayalite–magnetite–quartz buffer; IW, iron–wustite buffer.

suggesting that this metamorphism may be related to the tectono–magmatic event that formed the HF basalts. All of this indicates that the HF basalts formed between 1529 and 1182 Ma.

Zuo et al. (2002) and Yan (2014) suggested that the AF and HF units of the Zhulongguan Group formed as a result of the intracontinental rifting that has been identified in neighboring regions (e.g., the Tarim Craton, the Qaidam Block, the North China Craton, and the Dunhuang Block). All of these regions record latest Paleoproterozoic to Mesoproterozoic rifting events (e.g., Peng et al., 2010; Lu et al., 2010). The geochemistry of the AF and Group I HF basalts are indicative of formation from a mantle plume in an intraplate environment (Fig. 11). This suggests that these basalts formed in an intracontinental rift during the early Mesoproterozoic.

The Group II HF basalts have N-MORB-like geochemical affinities and more depleted $\varepsilon_{Nd}(t)$ and $\varepsilon_{Hf}(t)$ isotopic compositions than the AF and Group I HF basalts (Figs. 6–8 and 12), indicating derivation from a

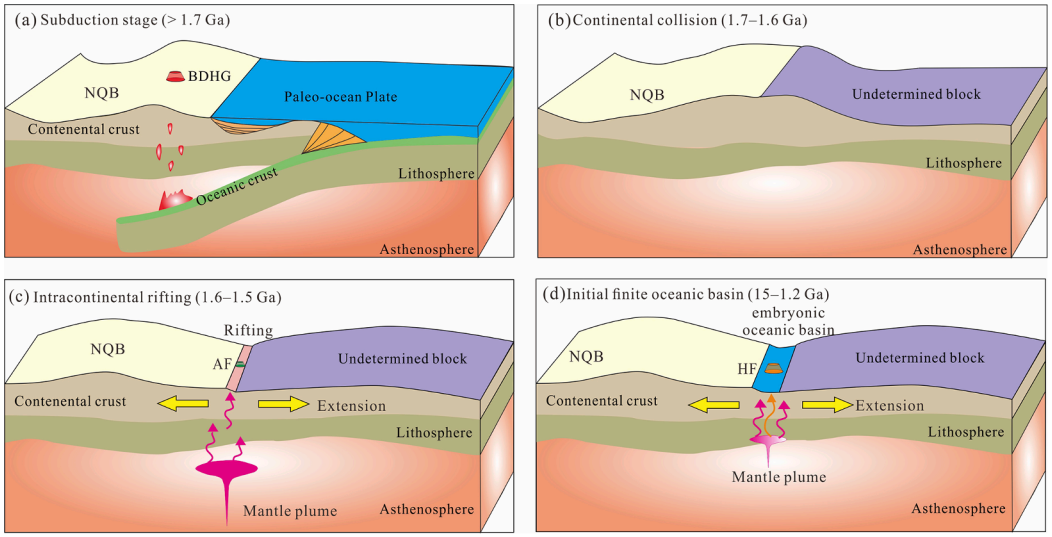

Fig. 14. Tectonic evolution of the North Qilian Block during the Paleoproterozoic–Mesoproterozoic.

depleted source region. The HF basalts are hosted by an argillaceous slate–carbonate–banded iron formation sequence that was deposited in a shallow sea sedimentary environment (Direen and Crawford, 2003). This suggests that the Group II HF basalts formed in an extensional tectonic setting similar to the limited oceanic basins that formed in this area during the middle Mesoproterozoic.

5. Proterozoic tectono–magmatic evolution of the western NQB

Previous studies have determined that the Columbia supercontinent was formed during the Paleoproterozoic (*ca.* 1.8 Ga; Rogers and Santosh, 2009). The development of 1.6–1.2 Ga intracontinental rift zones and the anorogenic magmatism (including rapakivi granites, kimberlites, lamproites, anorthosite–mangerite–charnockite–granite suites, and carbonatites) that is recorded in numerous cratonic blocks globally are all thought to provide evidence of the separation and fragmentation of Columbia (Zhao et al., 2016; Ernst and Bell, 2010). The new data presented in this study indicate that the NQB records late Paleoproterozoic to Mesoproterozoic tectono–magmatic events that have been identified in adjacent blocks (e.g., the North China and Tarim cratons, and the Middle Qilian, Dunhuang, and South China blocks; Guo et al., 1999; Lu et al., 2010; Zhao et al., 2016; Liu et al., 2019; Wang et al., 2020). The evolution of the NQB is also a response to the Columbia convergence and breakup processes that have been identified in North America, South America, Australia, and India (e.g., Pidgeon and Nemchin, 2001; Hou et al., 2008). All of this allows the tectonic evolution of the NQB to be summarized as follows (Fig. 14).

(1) A late Paleoproterozoic oceanic subduction stage (>1.74 Ga, Fig. 14a) involving the formation of the (meta-)mafic rocks of the BDHG in a continental arc setting, including units in the NQB, the Huangyuan Group of the Middle Qilian Block, and the Dunhuang Group of the Dunhuang Block (Guo et al., 1999; Zhao et al., 2015, 2017; this study). These tectono–magmatic events were a response to the convergence of the Columbia supercontinent (Rogers and Santosh, 2009).
(2) A paleo-oceanic closure and continental collisional stage (1.7–1.6 Ga, Fig. 14b) following the closure of a paleo-ocean and a series of subsequent late Paleoproterozoic orogenic events (Zhao et al., 2016). These involved the collision of the NQB with another plate (e.g., the North China Craton) during the latest Paleoproterozoic, as evidenced by the Lvliang–Zhongtiao orogeny of the North China Craton (Lu et al., 2010).
(3) A continental disintegration stage (1.6–1.5 Ga; Fig. 14c) where the NQB was involved in the start of a new Wilson cycle. This is evidenced by the formation of widespread early Mesoproterozoic OIB-like units (e.g., the AF and Group I HF basalts), mafic dikes, and A-type granites (e.g., Zuo et al., 2002; Gao, 2003; Peng et al., 2010; Wu et al, 2014; this study). This magmatism provides evidence of intracontinental rifting in the North China Craton, the Tarim Craton, and the NQB.
(4) An embryonic oceanic basin stage (1.5–1.2 Ga; Fig. 14d) where the rifting outlined above led to the formation of an embryonic oceanic basin and the generation of the Group II HF basalts. This is further evidenced by the formation of the Jingtieshan banded iron formations and associated metasedimentary rocks (*ca.* 1.2 Ga) in the North Qilian Orogenic Belt, all of which formed in an extensional setting in a continental marginal sea environment (Yang et al., 2016).

The last two stages are associated with large-scale breakup events recorded in the North China Craton (1.77–1.3 Ga) and the disintegration of the Columbia supercontinent (1.6–1.2 Ga; Rogers and Santosh, 2009). This also provides evidence that mantle plume activity was a key driver of the breakup of the Columbia supercontinent (Zhang et al., 2018).

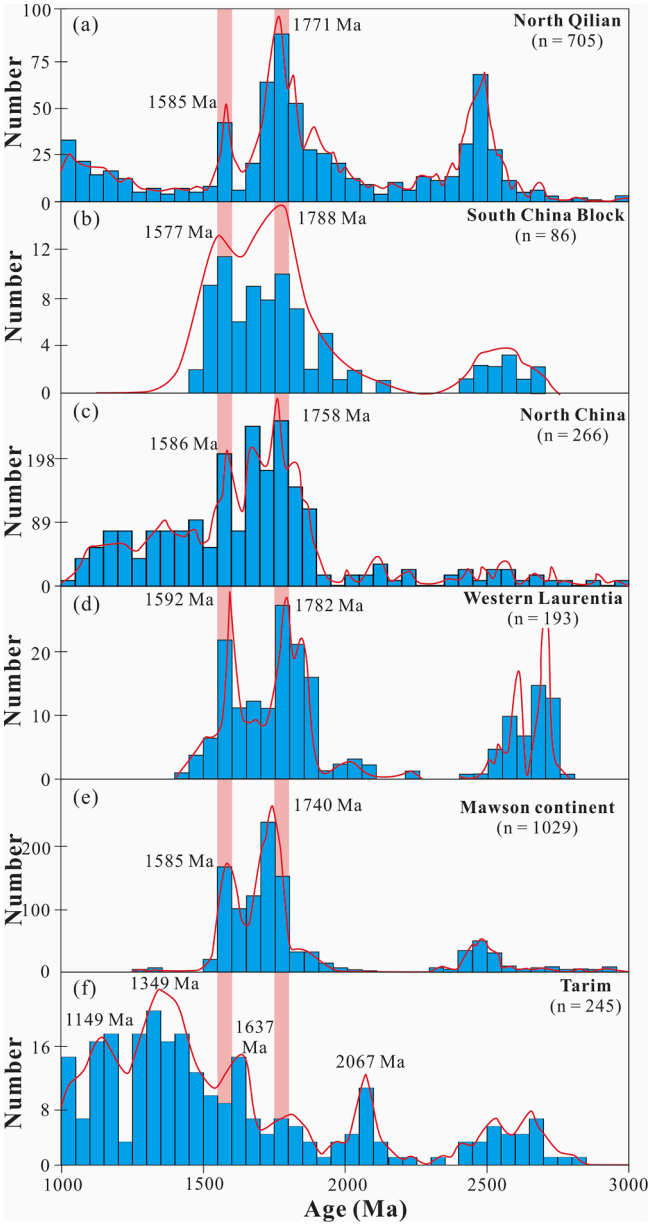

Fig. 15. U–Pb age spectra for detrital zircons from (a) the North Qilian Block (Xu et al., 2010; Gong et al., 2017; Liang et al., 2020); (b) the South China Block (Xu et al., 2019), (c) the North China Craton (Kang et al., 2020), (d) the western Laurentia (Ross and Villeneuve, 2003), (e) the Mawson continent (Cherry et al., 2017) and (f) the Tarim Craton (Wang et al., 2020).

6. Location of the NQB within the Columbia supercontinent

The above considerations indicate that the NQB was part of the Columbia supercontinent, with Laurentia occupying a central location (e.g., Zhang et al., 2012; Pisarevsky et al., 2014; Zhao et al., 2016), which flanked by the South America–West Africa, the Western Australia–South Africa, the East Antarctica, and the North China–India (Zhao et al., 2004). The western Laurentia contained a widespread thick Mesoproterozoic basin sedimentary succession (e.g., the Belt–Purcell Supergroup and its equivalents) that has been used to constrain the nature of continental fragments to the west of Laurentia (e.g., Hou et al., 2008). These basin deposits are characterized by 1.6–1.5 Ga detrital zircons (Condie et al., 2009), which is inconsistent with there being two episodes of magmatism at 1.70–1.65 and 1.48–1.35 Ga, with a hiatus during 1.65–1.49 Ga (Stewart et al., 2010). However, this rare 1.6–1.5

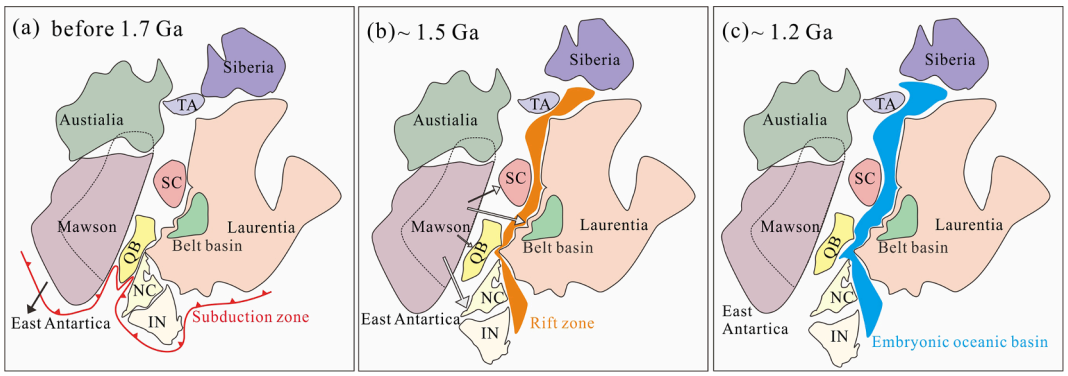

Fig. 16. Paleogeographic reconstruction showing the location of the Qilian Block within the Columbia supercontinent and the tectonic evolution of the Columbia supercontinent at (a) 1.7 Ga, (b) 1.5 Ga, and (c) 1.2 Ga (modified after Hou et al., 2008; Zhao et al., 2004). Abbreviations: IN (India Craton); NC (North China Craton); QB (Qllian Block); SC (South China Block) and TA (Tarcim Craton).

Ga magmatism occurred along the eastern margin of the northern Australia–Mawson continent (Condie et al., 2009), suggesting a 1.6–1.5 Ga sedimentary and tectonic link between the western Laurentia and the northern Australia–Mawson continent (i.e., part of the East Antarctica and Southern Australia; Jones et al., 2015). This is confirmed by the Australia–Mawson continent and Laurentia having similar polar-wander paths during the Paleoproterozoic, as indicated by the analogous Paleoproterozoic poles within these continents (Pisarevsky et al., 2014; Kirscher et al., 2019). Furthermore, paleocurrent data from the Belt-Purcell Supergroup indicate that they deviated from the western source of the Mawson continent (e.g., Ross and Villeneuve, 2003). Therefore, the location of blocks within the Columbia supercontinent may be determined by the presence of 1.6–1.5 Ga detrital zircons (e.g., Yao et al., 2017; Zhang et al., 2019; Xu et al., 2019). For example, the South China Block has been proposed as one of the continental candidates that lay adjacent to the western Laurentia, based on the presence of 1.6–1.5 Ga detrital zircons in the Mesoproterozoic Baoban Complex (Yao et al., 2017; Zhang et al., 2019) on Hainan Island, within the southern part of the block. This is further evidenced by the detrital zircon age distribution of the > 1.45 Ga Gezhencun succession of the South China Block, which is broadly comparable with that identified in the lower Belt–Purcell Supergroup in western Laurentia (Xu et al., 2019). The Hf isotopic compositions of Proterozoic detrital zircons from sedimentary rocks in the Qilian and South China blocks indicate that the Qilian Block had a close relationship with South China Block during the Proterozoic (Gao et al., 2021). Recent research indicates that the Tarim Craton was located between the South China and Siberian blocks in the northwest Laurentia (e.g., Wu et al., 2014; Wang et al., 2020), and the North China and India cratons once lay to the southwest of the western Laurentia, based on reconstruction of the *ca.* 1.85 Ga giant radiating dyke swarm in the North China and India cratons and Laurentia (Hou et al., 2008).

Compiled detrital zircon data for the North Qilian and South China blocks, the North China and Tarim Cratons, the Mawson continent, and the western Laurentia are shown in Fig. 15. The timing of formation of the BDHG (*ca.* 1.74 Ga) and the AF (1.56–1.53 Ga), and age peaks (*ca.* 1.77 and 1.59 Ga) of detrital zircons from the North Qilian Block are similar to those of detrital zircons from the South China Block, the North China Craton, the western Laurentia, and the Mawson continent, all of which have Paleoproterozoic (*ca.* 1.79, 1.76, 1.78, and 1.74 Ga, respectively) and Mesoproterozoic (*ca.* 1.58, 1.59, 1.59, and 1.59 Ga, respectively) age peaks (Fig. 15a–e). However, detrital zircons from the Tarim Craton record episodic Meso- and Paleoproterozoic magmatism at *ca.* 1.15 and 1.35 Ga, and 1.64 and 2.07 Ga, respectively (Fig. 15f). This strongly suggests that the 1.6–1.5 Ga detrital zircons of the NQB, the South China Block, the North China Craton, and the western Laurentia were likely derived from the Mawson continent (Fig. 16). Given that there were rifts in the western Laurentia and subduction zone in the southwestern Laurentia during the Proterozoic (Hou et al., 2008), with a subduction zone existing in the NQB as indicated by the IAB-like BDHG amphibolites (1740 ± 16 Ma). The NQB and the North China Craton lay to the southwest of Laurentia within the Columbia supercontinent during the Paleoproterozoic–Mesoproterozoic (Fig. 16). The Paleo–Mesoproterozoic tectono–magmatism in the NQB was a response to the convergence and breakup of the Columbia supercontinent, providing insight to the tectonic evolution of the Columbia supercontinent. In the Paleoproterozoic, the BDHG was formed in a continental arc setting, indicating the convergence of the Columbia supercontinent with an external subduction zone (Fig. 16a; Zhao et al., 2004; Hou et al., 2008). This was followed by rifting between the Laurentia and other blocks due to the breakup of the Columbia supercontinent during the early Mesoproterozoic (Fig. 16b). The embryonic oceanic basin was then formed during the late Mesoproterozoic (Fig. 16c).

7. Conclusions

The new zircon U–Pb geochronological, geochemical, and isotopic data for the Beidahe and Zhulongguan groups samples presented in this study further our understanding of the Paleoproterozoic–Mesoproterozoic formation, petrogenesis, and tectonic evolution of the North Qilian Block, all of which are associated with the formation and breakup of the Columbia supercontinent. The main findings of this study are as follows.

(1) IAB-like BDHG amphibolites were derived from a metasomatized mantle wedge source in a continental arc setting during the Paleoproterozoic (1740 ± 16 Ma).
(2) Quartz-biotite schists in the lower part of the AF yield a magmatic zircon $^{207}Pb/^{206}Pb$ weighted mean age of 1555 ± 9 Ma. Basalts in the AF have OIB-like compositions and formed as a result of mantle plume magmatism in an intracontinental rift setting.
(3) Group I HF basalts have OIB-like compositions and formed as a result of mantle plume magmatism in an intracontinental rift setting, whereas the Group II HF basalts have N-MORB-like compositions and formed in an embryonic oceanic basin setting.
(4) Paleoproterozoic–Mesoproterozoic tectono–magmatic events in the NQB reflect the convergence and breakup of the Columbia supercontinent where the evolution of the NQB represents a microcosm of the tectonic events that affected the supercontinent. The NQB was most likely located to the southwest of Laurentia, within the Columbia supercontinent.

Declaration of Competing Interest

The authors declare that they have no known competing financial interests or personal relationships that could have appeared to influence

the work reported in this paper.

Acknowledgements

We are grateful to the anonymous reviewers for their careful reviews and constructive comments, and thank Prof. Guo-Chun Zhao for his editorial handling of this paper. This study was financially supported by research grants from Second Tibetan Plateau Scientific Expedition and Research Program (2019QZKK0703), National Key Research and Development Project of China (2020YFA0714804), National Science Foundation of China (41873037, 92055206), Comprehensive Study on Characteristics of Sedimentary Metamorphic Iron Ores in Kawa Exploration Area, Sunan County, Gansu Province (Grant No. Gan Caijian 2014–99) and Foundation of Basic Scientific Research of Central Universities (Grant No. lzujbky–2018–it20).

Appendix A. Supplementary data

Supplementary data to this article can be found online at https://doi.org/10.1016/j.precamres.2021.106424.

References

Brenan, J.M., Shaw, H.F., Ryerson, F.J., Phinney, D.L., 1995. Mineral–aqueous fluid partitioning of trace elements at 900°C and 2.0 GPa: constraints on the trace element chemistry of mantle and deep crustal fluids. Geochim. Cosmochim. Acta 59 (16), 3331–3350. https://doi.org/10.1016/0016-7037(95)00215-L.

Cherry, A.R., McPhie, J., Kamenetsky, V.S., Ehrig, K., Keeling, J.L., Kamenetsky, M.B., Meffre, S., Apukhtina, O.B., 2017. Linking Olympic Dam and the Cariewerloo Basin: was a sedimentary basin involved in formation of the world's largest uranium deposit. Precambr. Res. 300, 168–180. https://doi.org/10.1016/j.precamres.2017.08.002.

Chauvel, C., Lewin, E., Carpentier, M., Arndt, N.T., Marini, J.C., 2008. Role of recycled oceanic basalt and sediment in generating the Hf–Nd mantle array. Nat. Geosci. 1 (1), 64–67. https://doi.org/10.1038/ngeo.2007.51.

Condie, K.C., Belousova, E., Griffn, W.L., Sircombe, K.N., 2009. Granitoid events in space and time. Constraints from igneous and detrital zircon age spectra. Gondwana Res. 15 (3–4), 228–242. https://doi.org/10.1016/j.gr.2008.06.001.

Direen, N.G., Crawford, A.J., 2003. Fossil seaward–dipping reflector sequences preserved in southeastern Australia: a 600 Ma volcanic passive margin in eastern Gondwanaland. J. Geol. Soc. 160, 985–990. https://doi.org/10.1144/0016-764903-010.

Ernst, R.E., Bell, K., 2010. Large igneous provinces (LIPs) and carbonatites. Mineral. Petrol. 98 (1–4), 55–76. https://doi.org/10.1007/s00710-009-0074-1.

Frost, D.J., Mccammon, C.A., 2008. The Redox State of Earth's Mantle. Annu. Rev. Earth Planet. Sci. 36 (1), 389–420. https://doi.org/10.1146/annurev.earth.36.031207.124322.

Fu, G.M., Su, J.P., Hu, N.G., 2005. Geochemical characteristics and tectonic setting of amphibolites in the Paleoproterozoic Beidahe Group in the western part of the Qilian Orogenic Belt. Geol. China 32 (4), 541–547 (in Chinese with English abstract).

Gao, Y.L., Long, X.P., Luo, J., Dong, Y.P., Lan, C.Y., Huang, Z.Y., Zhao, J., 2021. Provenance and Hf isotopic variation of Precambrian detrital zircons from the Qilian Orogenic Belt, NW China: evidence to the transition from breakup of Columbia to the assembly of Rodinia. Precambr. Res. 106153 https://doi.org/10.1016/j.precamres.2021.106153.

Gao, Y.Q., 2003. Study on the characteristics of protolith formation and tectonic environment of BDHG in the West Qilian. Doctoral thesis, Chang'An University. https://doi.org/10.7666/d.Y559043 (in Chinese).

Gong, H., Zhao, H., Xie, W., Kang, W., Zhang, R., Yang, L., 2017. Tectono-thermal events of the north qilian orogenic belt, nw china: constraints from detrital zircon u-pb ages of heihe river sediments. J. Asian Earth Sci. 138 (MAY1), 647–656. https://doi.org/10.1016/j.jseaes.2017.03.003.

Guo, J.J., Zhao, F.Q., Li, H.K., 1999. Geological significance of the Jinning period collision type granite in the Eastern Middle Qilian. Acta Geosci. Sinica 20 (01), 10–15. https://doi.org/10.3321/j.issn:1006-3021.1999.01.002.

Haase, K.M., Devey, C.W., 1996. Geochemistry of lavas from the Ahu and Tupa volcanic fields, Easter Hotspot, southeast Pacific: implications for intraplate magma genesis near a spreading axis. Earth Planet. Sci. Lett. 137 (1), 129–143. https://doi.org/10.1016/0012-821X(95)00217-Z.

Herzberg, C., Asimow, P.D., 2015. PRIMELT3 MEGA.XLSM software for primary magma calculation: Peridotite primary magma MgO contents from the liquidus to the solidus. Geochem. Geophys. Geosyst. 16 (2), 563–578. https://doi.org/10.1002/2014gc005631.

Hou, G.T., Santosh, M., Qian, X.L., Gordon, S., 2008. Tectonic constraints on 1.3–1.2 Ga final breakup of Columbia supercontinent from a giant radiating dyke swarm. Gondwana Res. 14, 561–566. https://doi.org/10.1016/j.gr.2008.03.005.

Jackson, M.G., Kurz, M.D., Hart, S.R., Workman, R.K., 2007. New Samoan lavas from Ofu Island reveal a hemispherically heterogeneous high $^{3}He/^{4}He$ mantle. Earth Planet. Sci. Lett. 264, 360–374. https://doi.org/10.1016/j.epsl.2007.09.023.

Jones, J.V., Daniel, C.G., Doe, M.F., 2015. Tectonic and sedimentary linkages between the Belt-Purcell basin and southwestern Laurentia during the Mesoproterozoic, ca. 1.60–1.40 Ga. Lithosphere 7 (4), 465–472. https://doi.org/10.1130/L438.1.

Kang, Y., Chen, G., Chen, Q., Yang, F., Xia, X., 2020. Detrital zircon ages, sources, and implications of the Tangwangling Group, southern margin of the Ordos Block, western North China Craton. Geosci. J. 25 (2), 107–124. https://doi.org/10.1007/s12303-020-0016-9.

Kelemen, P.B., Yogodzinski, G.M., Scholl, D.W., Scholl, D.W., 2003. Along-strike variation in the Aleutian island arc: genesis of high Mg# andesite and implications for continental crust. Washington Dc Am. Geophys. Union Geophys. Monogr. 138 (1), 223–276. https://doi.org/10.1029/138GM11.

Kempton, P.D., Pearce, J.A., Barry, T.L., Fitton, J.G., Langmuir, C., Christie, D.M., 2002. Sr–Nd–Pb–Hf Isotope Results from ODP Leg 187: evidence for mantle dynamics of the Australian-Antarctic discordance and origin of the Indian MORB source. Geochem. Geophys. Geosyst. 3 (12), 1–35. https://doi.org/10.1029/2002GC000320.

Kessel, R., Schmidt, M.W., Ulmer, P., Pettke, T., 2005. Trace element signature of subduction-zone fluids, melts and supercritical liquids at 120–180 km depth. Nature 439 (7059), 724–727. https://doi.org/10.1038/nature03971.

Kirscher, U., Liu, Y., Li, Z.X., Mitchell, R.N., Pisarevsky, S.A., Denyszyn, S.W., Nordsvan, A., 2019. Paleomagnetism of the Hart Dolerite (Kimberley, Western Australia): a two-stage assembly of the supercontinent Nuna. Precambr. Res. 329, 170–181. https://doi.org/10.1016/j.precamres.2018.12.026.

Lee, C.T., Luffi, P., Plank, T., Dalton, H., Leeman, W., 2009. Constraints on the depths and temperatures of basaltic magma generation on Earth and other terrestrial planets using new thermobarometers for mafic magmas. Earth Planet. Sci. Lett. 279 (1–2), 2020–3333. https://doi.org/10.1016/j.epsl.2008.12.020.

Liang, J.W., Ma, X.J., Tao, W.X., 2020. Detrital zircon u-pb ages of middle-late permian sedimentary rocks from the southwestern margin of the north china craton: implications for provenance and tectonic evolution. Gondwana Res. 88 https://doi.org/10.1016/j.gr.2020.07.008.

Litvak, V.D., Poma, S., 2010. Geochemistry of mafic Paleocene volcanic rocks in the Valle del Cura region: Implications for the petrogenesis of primary mantle-derived melts over the Pampean flat-slab. J. S. Am. Earth Sci. 29, 705–716. https://doi.org/10.1016/j.jsames.2010.01.001.

Liu, K., Lu, G., Wang, Z., Huang, S., Wang, W., 2019. The Paleoproterozoic bimodal magmatism in the SW Yangtze Block: implications for initial breakup of the Columbia supercontinent. Lithos 332–333, 23–38. https://doi.org/10.1016/j.lithos.2019.02.021.

Lu, S.N., Li, H.K., Xiang, Z.Q., 2010. A review of the research progress of isotopic geochronology in Mesoproterozoic China. Chin. Geol. 37 (4), 1002–1013. https://doi.org/10.3969/j.issn.1000-3657.2010.04.015.

Merle, R., Marzoli, A., Reisberg, L., Bertrand, H., Nemchin, A., Chiaradia, M., Callegaro, S., Jourdan, F., 2014. Sr, Nd, Pb and Os isotope systematics of CAMP tholeiites from Eastern North America (ENA): evidence of a subduction–enriched mantle source. J. Petrol. 55 (1), 133–180. https://doi.org/10.1093/petrology/egt063.

Nan, Y.C., 2018. The characteristics and original rock recovery of Beidahe rock group b petrofabric metamorphic rock in Daquan Area Western Qilian Mountain. Master's dissertation, Chengdu University of Technology (in Chinese).

Nielsen, S.G., Marschall, H.R., 2017. Geochemical evidence for mélange melting in global arcs. Sci. Adv. 3 (4) https://doi.org/10.1126/sciadv.1602402.

Pearce, J.A., Norry, M.J., 1979. Petrogenetic implications of Ti, Zr, Y, and Nb variations in volcanic rocks. Contrib. Miner. Petrol. 69 (1), 33–47. https://doi.org/10.1007/BF00375192.

Peng, P., Guo, J., Zhai, M., Bleeker, W., 2010. Paleoproterozoic gabbronoritic and granitic magmatism in the northern margin of the North China Craton: evidence of crust–mantle interaction. Precambr. Res. 183 (3), 635–659. https://doi.org/10.1016/j.precamres.2010.08.015.

Pidgeon, R.T., Nemchin, A.A., 2001. 1.2 Ga Mafic dyke near York, southwestern Yilgarn Craton, Western Australia. Aust. J. Earth Sci. 48, 751–755. https://doi.org/10.1046/j.1440-0952.2001.485895.x.

Pisarevsky, S.A., Elming, S.A., Pesonen, L.J., Li, Z.-X., 2014. Mesoproterozoic paleogeography. Supercontinent and beyond. Precambr. Res. 244, 207–225. https://doi.org/10.1016/j.precamres.2013.05.014.

Plank, T., Langmuir, C.H., Albarede, F., 1998. The chemical composition of subducting sediment and its consequences for the crust and mantle. Chem. Geol. 145 (3–4), 325–394. https://doi.org/10.1016/S0009-2541(97)00150-2.

Polat, A., Hofmann, A.W., 2003. Alteration and geochemical patterns in the 3.7–3.8 Ga Isua greenstone belt, West Greenland. Precambr. Res. 126, 197–218. https://doi.org/10.1016/S0301-9268(03)00095-0.

Qi, R.R., Chen, S.Q., Hu, X.C., 2015. The exploration practice of Jingtieshan iron ore deposit in the Western North Qilian, Gansu: an example of mining breakthrough in the rich area of Kawa iron ore. Gansu Geol. 24 (1), 11–18 (in Chinese with English abstract).

Rogers, J.J.W., Santosh, M., 2009. Tectonics and surface effects of the Supercontinent Columbia. Gondwana Res. 15 (3–4), 373–380. https://doi.org/10.1016/j.gr.2008.06.008.

Ross, G.M., Villeneuve, M., 2003. Provenance of the Mesoproterozoic (1.45 Ga) Belt basin (western North America): another piece in the pre-Rodinia paleogeographic puzzle. Geol. Soc. Am. Bull. 115 (10), 1191–1217. https://doi.org/10.1130/B25209.1.

Rudnick, R.L., Fountain, D.M., 1995. Nature and composition of the continental crust: a Lower crustal perspective. Rev. Geophys. 33 (3), 266–310. https://doi.org/10.1029/95rg01302.

Song, S.G., Niu, Y.L., Su, L., Xia, X., 2013. Tectonics of the North Qilian orogeny, NW China. Gondwana Res. 23 (4), 1378–1401. https://doi.org/10.1016/j.gr.2012.02.004.

Stewart, E.D., Link, P.K., Fanning, C.M., Frost, C.D., McCurry, M., 2010. Paleogeographic implications of non-North American sediment in the Mesoproterozoic upper Belt Supergroup and Lemhi Group, Idaho and Montana, USA. Geology 38 (10), 927–930. https://doi.org/10.1130/G31194.1.

Sun, S.S., McDonough, W.F., 1989. Chemical and isotopic systematics of oceanic basalts: implications for mantle composition and processes. Geol. Soc. London Spec. Publ. 42 (1), 313–345. https://doi.org/10.1144/GSL.SP.1989.042.01.19.

Tollstrup, D.L., Gill, J.B., 2005. Hafnium systematics of the Mariana arc: evidence for sediment melt and residual phases. Geology 33, 737–740. https://doi.org/10.1130/G21639.1.

Wang, C.Y., Zhang, Q., Qian, Q., 2005. Geochemistry of the Early Paleozoic Baiyin Volcanic Rocks (NW China): implications for the tectonic evolution of the North Qilian Orogenic Belt. J. Geol. 113 (1), 83–94. https://doi.org/10.1086/425970.

Wang, N., Wu, C.L., Lei, M., Chen, H.J., 2018. Petrogenesis and tectonic implications of the Early Paleozoic granites in the western segment of the North Qilian orogenic belt, China. Lithos 312–313, 89–107. https://doi.org/10.1016/j.lithos.2018.04.023.

Wang, P., Zhao, G.C., Liu, Q., Han, Y., Yao, J., Li, J., 2020. Zircons from the tarim basement provide insights into its positions in Columbia and Rodinia supercontinents. Precambr. Res. 341 https://doi.org/10.1016/j.precamres.2020.105621.

Winchester, J.A., Floyd, P.A., 1976. Geochemical magma type discrimination: application to altered and metarnorphosed basic igneous rocks. Earth Planet. Sci. Lett. 28, 459–469. https://doi.org/10.1016/0012-821x(76)90207-7.

Wu, C.Z., Santosh, M., Chen, Y.J., Samson, I.M., Lei, R.X., Dong, L.H., 2014. Geochronology and geochemistry of Early Mesoproterozoic meta–diabase sills from Quruqtagh in the northeastern Tarim Craton: implications for breakup of the Columbia supercontinent. Precambr. Res. 241, 29–43. https://doi.org/10.1016/j.precamres.2013.11.007.

Xia, X.H., Sun, N., Song, S.G., 2012. Age and tectonic setting of the Aoyougou-Erzhihaladaban ophiolite in the Western North Qilian Mountains, NW China. Acta Sci. Nat. Univ. Pekinensis 48 (5), 757–769. https://doi.org/10.13209/j.0479-8023.2012.099.

Xiang, Z.Q., Lu, S.N., Li, H.K., 2007. SHRIMP U-Pb zircon age of gabbro in Aoyougou in the western segment of the North Qilian Mountains, China and its geological implications. Geol. Bull. China 26 (12), 1686–1691. https://doi.org/10.3969/j.issn.1671-2552.2007.12.023.

Xu, X., Song, S.G., Su, L., Niu, Y.L., 2015. The 600–580 Ma continental rift basalts in North Qilian Shan, northwest China: Links between the Qilian-Qaidam block and SE Australia, and the reconstruction of East Gondwana. Precambr. Res. 257, 47–64. https://doi.org/10.1016/j.precamres.2014.11.017.

Xu, Y.G., He, B., Chung, S.L., Menzies, M.A., Frey, F.A., 2004. Geologic, geochemical, and geophysical consequences of plume involvement in the Emeishan flood-basalt province. Geology 32 (10), 917–920. https://doi.org/10.1130/G20602.1.

Xu, Y.J., Cawood, P.A., Zhang, H.C., Zi, J.W., Du, Y.S., 2019. The mesoproterozoic baoban complex, south china: a missing fragment of western Laurentian lithosphere. Geol. Soc. Am. Bull. 132 (7–8) https://doi.org/10.1130/B35380.1.

Xu, Y.J., Du, Y., Cawood, P.A., Yang, J., 2010. Provenance record of a foreland basin: detrital zircon U-Pb ages from Devonian strata in the North Qilian orogenic belt, China. Tectonophysics 495 (3–4), 337–347. https://doi.org/10.1016/j.tecto.2010.10.001.

Yan, J.H., 2014. The geochemistry and geochronology study of Aoyougou volcanic rock in Sunan County, Gansu province. Master's dissertation, Northwestern University (in Chinese).

Yang, F., Huang, X.L., Xu, Y.G., He, L., 2019. Plume-ridge interaction in the South China Sea, Thermometric evidence from Hole U1431E of IODP Expedition 349. Lithos 324–325, 466–478. https://doi.org/10.1016/j.lithos.2018.11.031.

Yang, X.Q., Zhang, Z., Guo, S., Chen, J., Wang, D., 2016. Geochronological and geochemical studies of the metasedimentary rocks and diabase from the jingtieshan deposit, north Qilian, NW China: constraints on the associated banded iron formations. Ore Geol. Rev. 73, 42–58. https://doi.org/10.1016/j.oregeorev.2015.10.018.

Yao, W., Li, Z.X., Li, W.X., Li, X.H., 2017. Proterozoic tectonics of Hainan Island in supercontinent cycles: new insights from geochronological and isotopic results. Precambr. Res. 290, 86–100. https://doi.org/10.1016/j.precamres.2017.01.001.

Yogodzinski, G.M., Brown, S.T., Kelemen, P.B., Vervoot, J.D., Maxim, P., Sims, K.W.W., Kaj, H., Jicha, B.R., Reinhard, W., 2015. The role of subducted basalt in the source of Island Arc Magmas: evidence from Seafloor Lavas of the Western Aleutians. J. Petrol. 3, 441–492. https://doi.org/10.1093/petrology/egv006.

Yu, B.D., 1997. New understanding of Changcheng Period stratigraphic division, Gansu. Gansu Geology 6 (01), 1–15 https://doi.org/CNKI:SUN:GSDZ.0.1997–01–000.

Zhang, L.M., Zhang, Y.Z., Cui, X., Cawood, P.A., Wang, Y.J., Zhang, A.M., 2019. Mesoproterozoic rift setting of SW Hainan: Evidence from the gneissic granites and metasedimentary rocks. Precambr. Res. 325, 69–87. https://doi.org/10.1016/j.precamres.2019.02.013.

Zhang, S., Li, Z.-X., Evans, D.A.D., Wu, H., Li, H., Dong, J., 2012. Pre-Rodinia supercontinent Nuna shaping up: a global synthesis with new paleomagnetic results from North China. Earth Planet. Sci. Lett. 353–354, 145–155. https://doi.org/10.1016/j.epsl.2012.07.034.

Zhang, Y.H., Ren, Z.Y., Hong, L.B., Zhang, Y., Zhang, L., Qian, S.P., Xu, Y.G., Chen, L.L., 2017. Differential partial melting process for temporal variations of Shandong basalts revealed by melt inclusions and their host olivines. Gondwana Res. 49, 205–221. https://doi.org/10.1016/j.gr.2017.05.019.

Zhang, Z.C., Mao, J.W., 1998. The geochemical characteristics and tectonic setting of the Proterozoic metamorphic volcanic rocks in the Western North Qilian. J. Mineral. Petrol. 18 (4), 22–30. https://doi.org/10.1038/sj.cr.7290029.

Zhang, N., Dang, Z., Huang, C., Li, Z.X., 2018. The dominant driving force for supercontinent breakup: Plume push or subduction retreat. Geosci. Front. 9, 997–1007. https://doi.org/10.1016/j.gsf.2018.01.010.

Zhao, G.C., Sun, M., Simon, W., Li, S.R., 2016. Assembly, accretion and break-up of the Paleo-Mesoproterozoic Columbia (Nuna) Supercontinent: Records in the North China Craton. Acta Geol. Sinica-Engl. Ed. 90 (s1), 50. https://doi.org/10.1111/1755-6724.12881.

Zhao, G.C., Sun, M., Wilde, S.A., Li, S.R., 2004. A Paleo-Mesoproterozoic Supercontinent: assembly, growth and breakup. Earth-Sci. Rev. 67 (1–2), 91–123. https://doi.org/10.1016/j.earscirev.2004.02.003.

Zhao, Y., Sun, Y., Diwu, C.R., Yan, J., 2015. The Archean-Paleoproterozoic crustal evolution in the Dunhuang region, NW China: constraints from zircon U-Pb geochronology and in situ Hf isotopes. Precambr. Res. 271, 83–97. https://doi.org/10.1016/j.precamres.2015.10.002.

Zhao, Y., Sun, Y., Diwu, C.R., Zhu, T., Ao, W., Zhang, H., 2017. Paleozoic intrusive rocks from the Dunhuang tectonic belt, NW China: constraints on the tectonic evolution of the Southernmost Central Asian Orogenic Belt. J. Asian Earth Sci. 38, 562–587. https://doi.org/10.1016/j.jseaes.2017.02.037.

Zuo, G.C., Liu, Y.K., Zhang, C., 2002. Tectonic stratigraphic characteristics of continental crust remnant groups in the middle western segment of North Qilian Orogenic Belt. Geol. Sci. 37 (3), 302–312 (in Chinese with English abstract).